



Enhancement of persulfate activation by Fe-biochar composites: Synergism of Fe and N-doped biochar

Peng Huang^a, Peng Zhang^{a,b,*}, Cuiping Wang^{a,b}, Jingchun Tang^{a,b}, Hongwen Sun^{a,b,*}

^a MOE Key Laboratory of Pollution Processes and Environmental Criteria, College of Environmental Science and Engineering, Nankai University, Tianjin 300350, China

^b Tianjin Engineering Center of Environmental Diagnosis and Contamination Remediation, Tianjin 300350, China

ARTICLE INFO

Keywords:

N-doped biochar
Zero-valent iron
Persulfate
Oxidation
Electron transfer

ABSTRACT

Persulfate-based (PS-based) advanced oxidation process is a promising technology for degradation of organic pollutants. PS activation needs efficient and economical catalysts and heterogeneous Fe-carbon composites are competitive. Herein, novel N-doped biochar-loaded nanoscale zero-valent iron (nZVI) composites (Fe@N-BC) were synthesized and evaluated for PS activation. Detailed characterization data indicated that graphitic and pyridine N structures were introduced by N-doping, which enhanced the anchoring, dispersion and loading of amorphous nZVI on biochar. Remarkably, the optimized Fe@N-BC material, Fe@N₂-BC₉₀₀, presented excellent catalytic performance for PS activation for lindane removal. The N-doped defects in biochar acted as reactive bridges and accelerated the electron transfer between nZVI and PS, showing strong synergistic effects toward nZVI. O₂^{•−} and ¹O₂ were the dominant active species in catalytic systems. Additionally, Fe@N₂-BC₉₀₀ catalyst showed effectiveness over a wide pH range for lindane removal. This work provides a new approach to the rational design and application of Fe@N-BC for persulfate activation in pollution control, which is certified by deep exploration of reaction mechanism.

1. Introduction

Advanced oxidation processes (AOPs) have been widely employed to rapidly and completely degrade organic pollutants in wastewater and groundwater via reactive oxygen species (ROSs) such as sulfate radicals (SO₄^{•−}) and hydroxyl radicals (•OH) [1,2]. In particular, AOPs based on persulfate (PS-based AOPs) have attracted much attention as an innovative oxidative treatment due to the relatively high stability, long-distance transmission and low cost of PS, and are expected to overcome the deficiencies of traditional AOPs [3–5]. PS needs external activation (e.g., UV, heat, microwave, transition metal ions and metal oxides) to break its critical O–O bond to produce ROSs with strong oxidation potential (mainly SO₄^{•−}, E₀ = 2.5–3.1 V) [5,6]. Activation of PS by transition metals is simpler, more efficient and economical than energy-based activation methods (e.g., thermal, UV, electrochemical, ultrasonic catalysis) [7,8]; therefore, has increasing application potential and attracts much attention.

Among all the tested transition metals, iron is the most preferred due to its abundant reserve, cost-effectiveness and environmental friendliness [9,10]. Generally, iron-based catalysts for PS activation can be

divided into two categories: homogeneous and heterogeneous catalysts. Heterogeneous iron-based catalysts show many advantages, such as good recyclability, wide pH response boundary, easy solid-liquid separation, and non-production of iron sludge [7, 11–13]. In recent years, nano- and micro-zero-valent iron (n(m)ZVI) has received particular attention for its ability to heterogeneously activate PS [14,15] and has widely been studied for the degradation of various organic pollutants (e.g., pesticides [16], polycyclic aromatic hydrocarbons [17], antibiotics [18,19]). However, the poor air stability, strong aggregation tendency, slow electron transfer cycle and low utilization of electrons of n(m)ZVI still constrain the efficiency of PS activation, and attempts need to be made to improve this approach [7,15,20].

Biochar, a new type of carbon-rich solid derived by pyrolyzing biomass under limited or no oxygen conditions, can behave as an effective carrier for transition metals including nZVI, which has been proved to be able to well distribute and protect nZVI to avoid reactivity defects [21–23]. It has been well documented that biochar-loaded nZVI composites exhibit higher catalytic activity than single ZVI since the biochar matrix can well distribute ZVI particles and can also participate in electron transfer and redox reactions due to its aromatic carbon [24].

* Correspondence to: Nankai University, 38# Tongyan Road, Haihe Education Park, Jinnan District, Tianjin 300350, China.

E-mail addresses: nkzhangpeng@nankai.edu.cn (P. Zhang), sunhongwen@nankai.edu.cn (H. Sun).

<https://doi.org/10.1016/j.apcatb.2021.120926>

Received 16 September 2021; Received in revised form 1 November 2021; Accepted 9 November 2021

Available online 16 November 2021

0926-3373/© 2021 Elsevier B.V. All rights reserved.

For instance, Yan et al. [25] reported that nZVI reactivity to generate $\text{SO}_4^{\bullet-}$ was significantly promoted with the support of rice hull-based biochar and the degradation of trichloroethylene was significantly enhanced. Moreover, a novel reaction path (nonradical pathway) of PS activation via electron transfer in Fe-biochar composites was proposed [26–28]. The preparation conditions (e.g., pyrolysis temperature, time) and precursors of biochar can affect its structural characteristics, leading to varied catalytic activity of the loaded nZVI and even change reaction pathways such as the radical and nonradical oxidation pathways [24, 27], which needs broad research to obtain an optimized performance.

Nitrogen is a fundamental component in biomass resources (e.g., straw, manure, and sludge waste), and the nitrogen atoms are trapped in the growing carbon network during pyrolyzing process, resulting in N-doped structures, such as pyridinic-N, pyrrolic-N and graphitic-N in biochar [29,30]. These N-doped structures in biochars can lead to changes in the charge distribution, bond structure and Lewis basic sites in the carbon network [31,32], thus may improving the loading, distribution and catalytic activity of nZVI and accelerating the reduction capacities of active sites and the electron transfer cycle between PS and catalysts [33,34]. For instance, Cai et al. [35] reported that biochar prepared with N-rich waste-bean dregs exhibited superior catalytic performance in PS activation for bisphenol A removal. However, most natural biomass materials (straw, wood) have low nitrogen contents in the range of 0.1%–5%, and the prepared biochars also have rare N-doped structures [30].

N-doping by extra N-dopants was claimed to be a promising approach to solve these problems [35]. For example, the synthesized Fe-N-C composite [26] and Fe/N codoped biochar [36] with additions of urea and dicyandiamide both showed good performance for PS activation. However, opposite results were also reported. Chen et al. [32] found that the N-doped active sites in biochar could be occupied or concealed by Fe species, which inhibited the synergistic catalytic effect in PS activation by Fe/N codoped biochar. Thus, due to the mistiness of diverse hybrid orbitals of N atoms in carbon network, the interactions among biochar, N-doped structures and Fe species have not been well clarified, and research on the effects of N-doping on the apparent structure formation or distribution of nZVI is also insufficient [37]. Therefore, further in-depth research is needed to accurately and fully explain the N-doping effects on biochar structure or nZVI distribution and the mechanism of PS activation to destruct organic pollutants.

Hence, in the present study, a series of novel Fe@N-BCs were synthesized by a combined route of pyrolysis and liquid phase reduction using different proportions of wood pulp, urea and ferric salt. The structure features of these composites were systematically characterized; particularly, the growth, anchoring and distribution of nZVI on the N-doped biochar and the effects of the N-doping were investigated. Owing to the characteristics of high toxicity, persistence, long-distance migration and hard-degradation, lindane (γ -hexachlorophene, γ -HCH) was selected as the target organic pollutant and its main properties are summarized in Table S1 in the Supporting Information (SI). Fe@N-BCs were used to activate PS for γ -HCH degradation under different conditions to optimize the degradation. To explore the underlying mechanism for γ -HCH degradation by Fe@N-BC-activated PS (Fe@N-BC/PS), chemical quenching experiments and electron paramagnetic resonance (EPR) detection for ROSs were both performed, and electrochemical analysis was also conducted to elucidate dynamic charge transfer between catalysts and PS intermediates.

2. Materials and methods

2.1. Biomass and chemicals

Dried wood pulp was used as the raw material for biochar production. Wood pulp is a kind of biomass derived from natural wood or plants after simple chemical treatment [38,39]. The wood pulp used in this study was purchased from Dalian Yangrun Trading Company (Dalian,

China) and was mainly composed of abundant cellulose with rare nitrogen (Bulk elemental composition: C: 42%, O: 49%, H: 8%, and N: 0.1% wt.). Gamma-hexachlorocyclohexane (γ -HCH, 99%) was purchased from Dr. Ehrenstorfer GmbH Company (Germany). Chemicals, including commercial ZVI (cZVI), urea, $\text{Na}_2\text{S}_2\text{O}_8$ (PS), $\text{FeSO}_4 \cdot 7\text{H}_2\text{O}$, NaNO_3 , NaH_2PO_4 , NaCl , NaHCO_3 and Na_2SO_4 were all obtained from Shanghai Meryer Chemical Technology Company (China). H_2SO_4 , NaOH , NaBH_4 , *n*-hexane, tert-butyl alcohol (TBA) and ethanol (EtOH) were purchased from Tianjin Bohai Chemical Industry Group Company (Tianjin, China). Humic acid (HA), 5,5-dimethyl-1-pyrroline-N-oxide (DMPO), 2,2,6,6-tetramethyl-4-piperidone (TEMP), *p*-benzoquinone (*p*-BQ) and *L*-histidine were provided by Shanghai Aladdin Bio-Chem Technology Company (China). All of the chemicals used in this study were of analytical or HPLC grade.

2.2. Preparation and characterization of Fe@N-BC composites

Dried wood pulp (1.0 g) was added into glass beakers and mixed with urea solutions (as N-dopant, 0, 0.5, 1.0 and 2.0 g urea in 50 mL deionized water) to make the mass ratios of urea and dried pulp of 0, 0.5, 1.0, and 2.0, respectively. The mixtures were stirred at 500 rpm for 4 h ($25 \pm 1^\circ\text{C}$) and then directly dried at 80°C in an air-dry oven. The obtained solid was pyrolyzed at 500, 700 and 900°C in an atmosphere-controlled furnace under N_2 atmosphere, which was heated with a rate of $5^\circ\text{C}/\text{min}$ and kept at designed temperature for 30 min. Finally, the furnace was slowly and naturally cooled to room temperature to obtain N-doped biochars (N-BCs) and was recorded as $\text{N}_m\text{-BC}_n$, with *m* indicating the N-doping content (0, 0.5, 1 and 2) and *n* indicating the pyrolysis temperature (500, 700 and 900°C) of biochars. The yielded N-BC materials were ground to pass through 60 mesh sieves for the preparation of Fe@N-BC composites in the next experiment.

The Fe@N-BC composites were prepared with modified versions of the methods described by Yan et al. [25] and Su et al. [40]. First, 0.756 g of the prepared N-BCs was suspended in 250 mL of 54 mM $\text{FeSO}_4 \cdot 7\text{H}_2\text{O}$ water solution in a glass beaker, sealed with film and stirred for 12 h. After adsorption saturation, the Fe^{2+} deposited on the N-BC surface was reduced to nZVI by dropwise addition of 250 mL of 108 mM NaBH_4 while stirred at 800 rpm. The mixture was then stirred for another 30 min and the solid particles were collected by filtration with a $0.22\ \mu\text{m}$ cellulose microporous filtration membrane. Finally, the collected Fe@N-BCs were subsequently washed with deionized water (200 mL) and ethanol (100 mL) and then freeze dried. The final products were stored in an anaerobic tank and were labeled as Fe@ $\text{N}_m\text{-BC}_n$ (the meaning of *m* and *n* is the same as above).

The morphology, structure and chemical composition of the prepared Fe@N-BC composites were characterized by bulk organic elemental analysis, field emission scanning electron microscopy (FE-SEM) with EDS element mapping, transmission electron microscopy (TEM) with selected area electron diffraction (SAED), X-ray diffraction (XRD), Fourier transform infrared spectroscopy (FTIR), nitrogen adsorption-desorption isotherms, and X-ray photoelectron spectroscopy (XPS). Details of these measures are presented in Text S1 of the SI.

2.3. γ -HCH degradation experiment

Prior to γ -HCH degradation experiments, the adsorption capacity of the pure biochars $\text{N}_{0.2}\text{-BC}_{900}$ was checked, and the results showed that the adsorption was less than 7.5% of the total spiked mass of γ -HCH within 180 min (Fig. S1). Hence, we can conclude that the removal of γ -HCH in Fe@N-BC suspensions with or without the addition of PS was deemed to be primarily caused by catalytic degradation.

Batch experiments of γ -HCH degradation were conducted in 40-mL amber glass vials containing 1.25 g/L catalyst, 4 mM PS, and 10 mg/L γ -HCH in 40 mL deionized water. The vials were placed on a shaker and horizontally shaken at 150 rpm and $25 \pm 1^\circ\text{C}$ for 360 min. At specific sampling times (0, 2, 5, 10, 30, 60, 120, 180 and 360 min), 0.5 mL of the

Table 1

Bulk elemental compositions and atomic ratios of Fe@N-BC composites.

Samples	Elemental compositions					Atomic ratios		
	C (%)	Fe (%)	O (%)	N (%)	H (%)	H/C	O/C	Fe/C
Fe@N ₀ -BC ₅₀₀	41.0 ± 0.3	43.2 ± 0.3	11.6 ± 0.1	1.58 ± 0.43	2.69 ± 0.28	0.79	0.19	0.23
Fe@N _{0.5} -BC ₅₀₀	35.0 ± 0.2	42.6 ± 0.2	15.1 ± 0.2	5.23 ± 0.19	2.08 ± 0.16	0.71	0.29	0.26
Fe@N ₁ -BC ₅₀₀	34.1 ± 0.1	47.5 ± 0.2	10.1 ± 0.2	6.27 ± 0.04	2.01 ± 0.02	0.71	0.20	0.30
Fe@N ₂ -BC ₅₀₀	32.7 ± 0.2	48.2 ± 0.2	9.57 ± 0.37	7.71 ± 0.06	1.80 ± 0.02	0.66	0.20	0.32
Fe@N ₀ -BC ₇₀₀	41.8 ± 0.3	49.8 ± 0.2	5.70 ± 0.28	1.02 ± 0.09	1.68 ± 0.15	0.48	0.09	0.26
Fe@N _{0.5} -BC ₇₀₀	37.5 ± 0.2	49.9 ± 0.1	6.66 ± 0.12	4.38 ± 0.06	1.54 ± 0.09	0.49	0.12	0.29
Fe@N ₁ -BC ₇₀₀	36.4 ± 0.4	49.9 ± 0.3	7.02 ± 0.10	5.33 ± 0.13	1.34 ± 0.12	0.44	0.13	0.29
Fe@N ₂ -BC ₇₀₀	36.4 ± 0.1	50.0 ± 0.1	6.56 ± 0.20	5.56 ± 0.12	1.47 ± 0.07	0.48	0.12	0.30
Fe@N ₀ -BC ₉₀₀	37.3 ± 0.2	48.7 ± 0.2	11.7 ± 0.1	1.04 ± 0.02	1.28 ± 0.04	0.41	0.21	0.28
Fe@N _{0.5} -BC ₉₀₀	35.3 ± 0.1	49.1 ± 0.3	11.7 ± 0.4	2.52 ± 0.02	1.45 ± 0.09	0.49	0.22	0.30
Fe@N ₁ -BC ₉₀₀	36.0 ± 0.3	48.1 ± 0.2	11.7 ± 0.2	2.81 ± 0.13	1.40 ± 0.06	0.47	0.22	0.29
Fe@N ₂ -BC ₉₀₀	38.2 ± 0.2	50.0 ± 0.1	7.47 ± 0.18	3.03 ± 0.01	1.37 ± 0.03	0.43	0.15	0.28

liquid phase was collected and mixed with 1.0 mL hexane in a 2.0-mL centrifuge tube. Then, the mixtures were oscillated by vortexing for 10 min and 0.5 mL of the supernatant was taken out after centrifugation at 5000 rpm for 2 min for analysis of residue γ -HCH. Prior to analysis, the supernatant was stored at -20°C . All experiments were conducted in triplicate.

Among the synthesized composites, Fe@N₂-BC₉₀₀ had the best performance, and optimization experiments for catalyst dosages (0.5–1.25 g/L), PS dosages (2–6 mM), pH values (3–11, adjusted with 0.1 mM NaOH and 0.1 mM H₂SO₄) were conducted using Fe@N₂-BC₉₀₀. Moreover, the influences of coexisting anions (NO₃[−], Cl[−], HCO₃[−] and H₂PO₄[−]) and the presence of HA on the γ -HCH catalytic degradation were also evaluated in the Fe@N₂-BC₉₀₀/PS system.

Furthermore, different quenching agents of EtOH, TBA, *p*-BQ and *L*-histidine were used to respectively determine the contributions of $\bullet\text{OH}$, SO₄^{•−}, O₂^{•−} and ¹O₂ to γ -HCH catalytic degradation. These ROSs were also detected by EPR spectroscopy (Bruker EMXplus-6/1, Germany) with DMPO and TEMP as spin-trapping agents in phosphate buffer solution (pH = 7.4), and detailed measurement procedure is shown in Text S2 of the SI. Electrochemical tests were conducted on a CHI 1040C electrochemical workstation (Shanghai Chenhua Instrument Company, China), which is described in Text S3 of the SI.

2.4. Analysis methods

The γ -HCH residue concentrations were determined by a 7890A GC (Agilent Corporation, USA), and the detailed procedure is shown in Text S4 of the SI. The concentrations of Fe²⁺ and PS in the aqueous phase of the catalytic systems were both determined by the 110-phenanthroline

and iodimetry methods described by Li et al. [26] and Liang et al. [41], respectively.

2.5. Data analysis

Degradation kinetic curves of γ -HCH were fitted using the pseudo-first-order kinetic model (Eq. 1):

$$\ln\left(\frac{C_0}{C_t}\right) = -k_{\text{obs}}t \quad (1)$$

where C_0 (mg/L) and C_t (mg/L) correspond to the γ -HCH concentrations at the initial state and at degradation time t (min), respectively; k_{obs} (min^{−1}) is the degradation rate constant.

All degradation data were analyzed using Origin 2018.

3. Results and discussion

3.1. Elemental compositions of catalysts

The result of bulk elemental compositions (Table 1) showed that all composites were mainly composed of C, Fe, O, N and H, and their mass percentages were in the order of Fe > C > O > N and H. The mass percentages of N in the composites significantly increased with increasing urea addition amounts (became slow at high N-dopant dosage), but significantly declined with increasing pyrolysis temperature ($p < 0.05$). Notably, the N mass percentage of Fe@N₂-BC₉₀₀ was 3.03%, which was 3 times that of Fe@N₀-BC₉₀₀. This result indicates that the N-doping successfully introduced N atoms into the biochar composites. Meanwhile, for Fe@N₀-2-BC₅₀₀, Fe mass percentage and atomic Fe/C ratio obviously increased while H/C ratios significantly

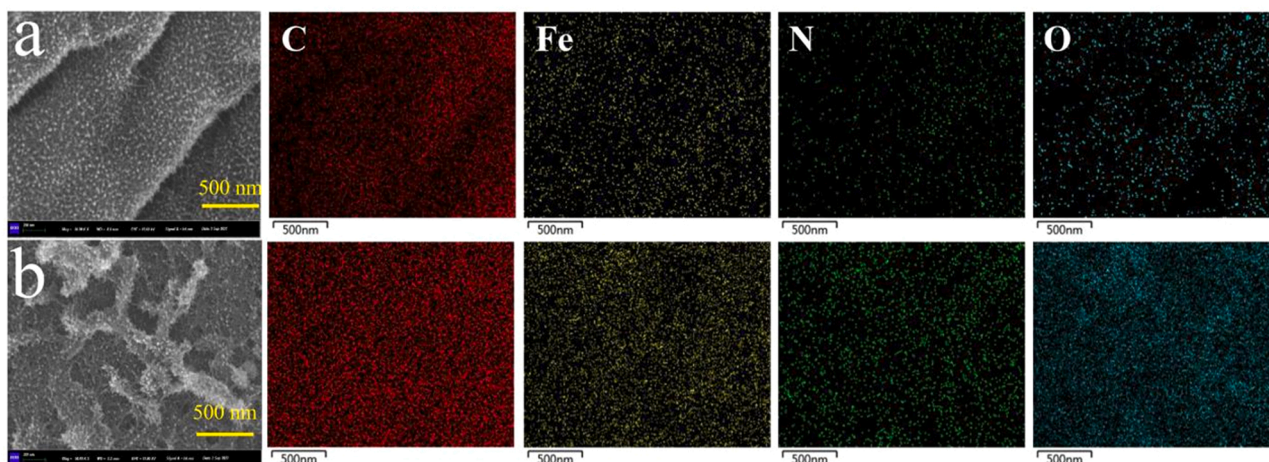


Fig. 1. SEM of N₀-BC₉₀₀ (a) and N₂-BC₉₀₀ (b) after Fe²⁺ adsorbing and their corresponding EDS elemental mappings of C, Fe, N and O elements.

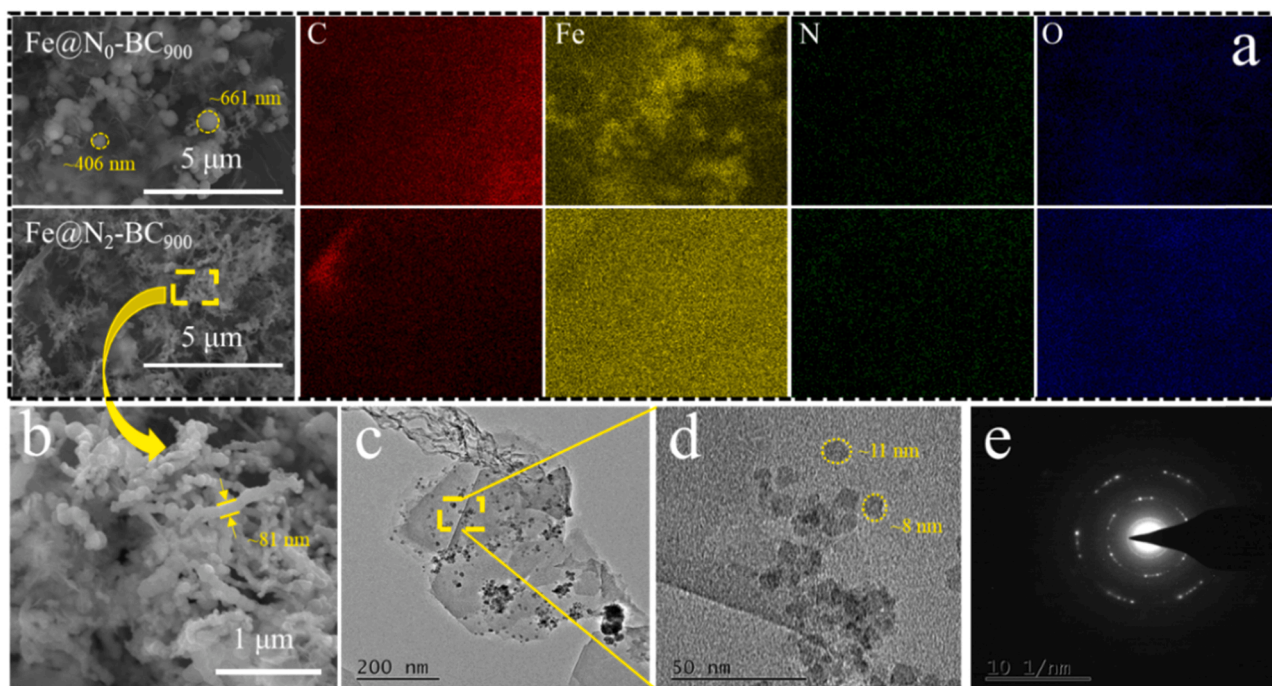


Fig. 2. SEM of Fe@N_{0.2}-BC₉₀₀ composites and their EDS elemental mappings of C, Fe, N and O elements (a); detailed morphology and structure (b), TEM image (c, d) and SAED images (g) of Fe@N₂-BC₉₀₀.

decreased with the increasing N mass percentage. However, the opposite result was obtained in Fe@N_{0.2}-BC_{700,900} that no significantly different Fe mass percentage was observed with the change in N mass percentage, which was due to that almost all of Fe (96.2–100%) in the liquid phase was deposited on biochar during the synthesis process of these Fe-biochar composites. These above findings suggest that N-doping significantly changes the elemental composition and aromaticity (H/C) of Fe-biochar composites, and these changes and Fe loading mass both became greater as the mass percentage of doped N increased.

The SEM images and EDS elemental mappings of N₀-BC₉₀₀ and N₂-BC₉₀₀ after Fe²⁺ adsorbing was examined to further clarify the effect of N-doping to the loading process of Fe on biochar. It can be seen from Fig. 1 that Fe²⁺ had been successfully adsorbed on the biochar surface. Meanwhile, compared to N₀-BC₉₀₀, N-doping enhanced the Fe²⁺ adsorption on N₂-BC₉₀₀ surface. This evidenced that Fe²⁺ was first anchored on the N-doping sites, and then in-situ reduced by NaBH₄ to

nZVI with higher dispersion and loading capacity on N-doped biochar.

3.2. Catalyst structure analysis

3.2.1. Morphology

SEM images and EDS elemental mappings of Fe@N_{0.2}-BC_{500–900} are shown in Figs. 2 and S1. As shown in Fig. 2a–b, it is clear that the presence of N corresponded to the C distribution in the architecture of Fe@N₂-BC₉₀₀ (Fig. 2a), suggesting that the N atoms were deeply embedded in the carbon network structure of the biochars by copolymerization. Furthermore, the nZVI on the Fe@N₀-BC₉₀₀ surface without N-doping aggregated into large spherical particles with diameters of 400–660 nm. While a nanowire or scattered distribution of particulate nZVI (diameter < 100 nm) appeared on the surface of N-doped Fe@N₂-BC₉₀₀, however, large spherical particles were also observed in the SEM images of Fe@N₂-BC_{500,700} (Fig. S2). This observation indicates that the

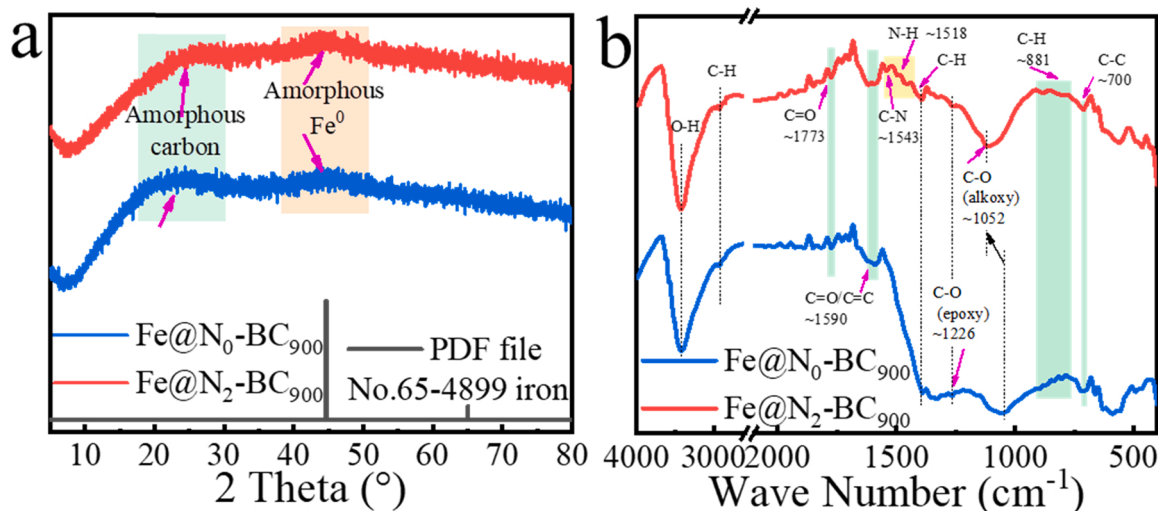


Fig. 3. XRD patterns (a), FTIR spectra (b) of Fe@N₀-BC₉₀₀ and Fe@N₂-BC₉₀₀.

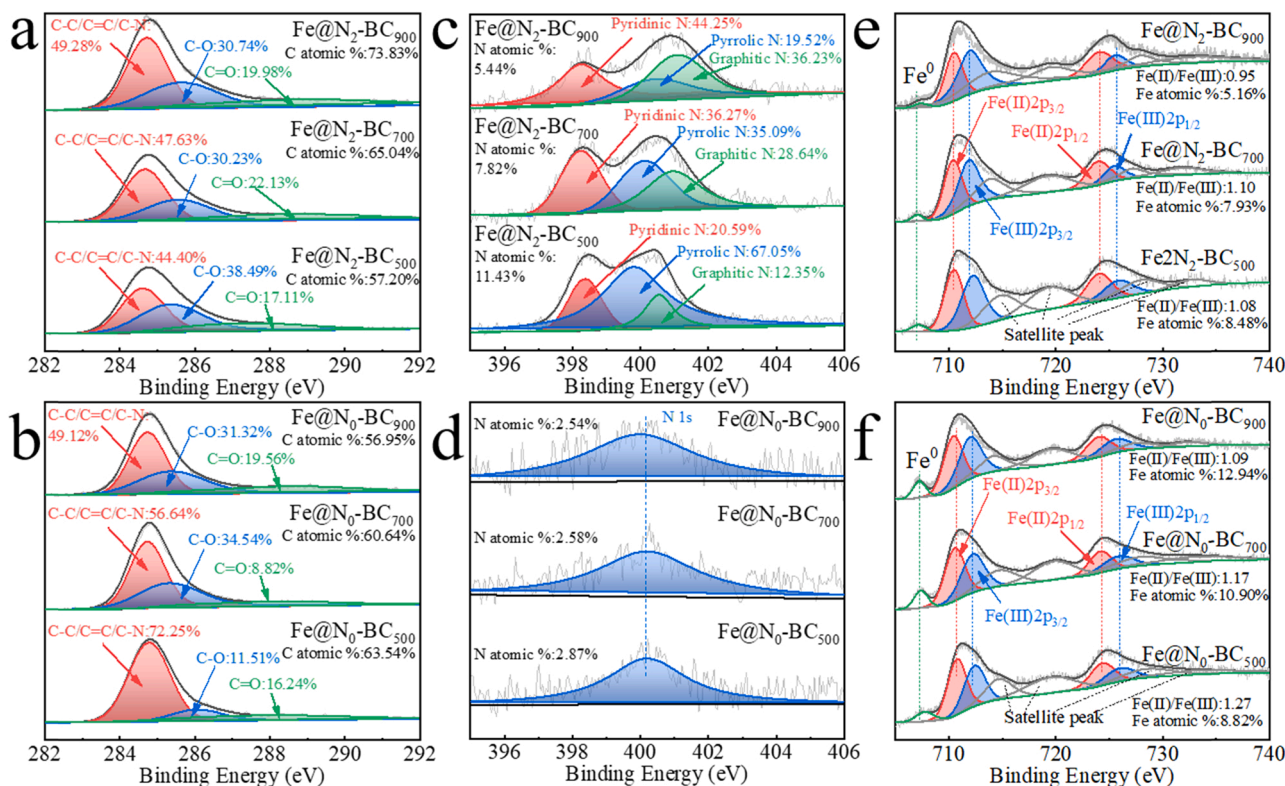


Fig. 4. High-resolution C1s (a–b), N1s (c–d) and Fe2p (e–f) XPS spectra of Fe@N_{0.2}-BC_{500–900}.

particle shape and size of nZVI on the composite surface changed with the pyrolysis temperature and the presence of doped N. Bright yellow areas of homogeneously distributed Fe nanoparticles or nanowires were clearly observed in Fe@N₂-BC₉₀₀, verifying that the N-doped biochar composite can prevent the agglomeration of nZVI and decrease its particle size. This result is consistent with the previous literature [26].

TEM images of Fe@N₂-BC₉₀₀ in Fig. 2c–d revealed that nZVI particles were scattered as black dots (5–25 nm) in the pore channels or carbon layers, indicating that some nZVI was present in the inner architecture. This can explain the decreased special surface area and micro- and mesopore volume of Fe@N-BC₉₀₀ (Fig. S3, Table S2). This geometrically interactive distribution of nZVI and the carbon layer and pore channel in Fe@N₂-BC₉₀₀ can not only suppress the agglomeration and oxidative consumption of nZVI but also enhance the interaction mode of electron transfer of the catalyst, thus promoting the catalytic reactivity [7]. Additionally, the SAED image (Fig. 2e) showed that nZVI in Fe@N₂-BC₉₀₀ was of amorphous structures.

3.2.2. XRD and FTIR analysis

To further investigate the crystal structure of the Fe@N-BC composites, XRD patterns of Fe@N_{0.2}-BC₉₀₀ were obtained (Fig. 3a). Two broad peaks at $2\theta = 19\text{--}26^\circ$ and 44° were observed and regarded as amorphous structures of carbon and Fe⁰, respectively [42], which is consistent with the SEM and TEM results in this study (Fig. 2). A similar amorphous structure was also observed in the XRD patterns of Fe@N_{0.2}-BC_{500,700}, but with weaker signals compared to Fe@N₂-BC₉₀₀ (Fig. S4). The amorphous Fe⁰ in the present study can be ascribed to the blocking effect of surface O- and N-containing functional groups on biochar during the reduction reaction of Fe²⁺ by NaBH₄ [42], which promoted the small crystalline size and good dispersion of Fe⁰ in the biochar carrier. Furthermore, the peak at the same location ($2\theta = 19\text{--}26^\circ$) was flatter for Fe@N₁₋₂-BC₉₀₀ (Fig. S4) compared to Fe@N₀-BC₉₀₀, verifying that N doping improved the crystallinity of the carbon in these composites.

As shown in the FTIR spectra (Fig. 3b), compared to Fe@N₀-BC₉₀₀,

two new peaks at 1543 and 1518 cm^{-1} were observed in Fe@N₂-BC₉₀₀, which were assigned to stretching vibration of C-N and N-H, indicating that N atoms were successfully doped in the carbon network structure of the biochar. Meanwhile, it is worth noting that after N-doping, the peak of the alkoxy C-O stretching vibration at 1052 cm^{-1} shifted to 1107 cm^{-1} in the Fe@N₂-BC₉₀₀ spectrum, which can be attributed to perceptible bond disorders and lattice distortion caused by the N-doping [31]. Furthermore, the vibration intensity of C-O decreased with increasing pyrolysis temperature of the biochar (Fig. S5). Hence, it is reasonable to speculate that the O atoms may be replaced from their original positions in the biochar by the N-doped structures (e.g., pyridinic-N, pyrrolic-N and graphitic-N) in the N-doping process.

3.2.3. XPS analysis

As shown in Fig. 4 and Table S3, C-C/C=C/C-N species were the primary components on the surface of all test composites with or without N-doping, and their relative contents in Fe@N₂-BC_{500–900} increased with increasing pyrolysis temperature (Fig. 4a), resulting from the formation of more C-N functional groups at higher pyrolysis temperatures (900°C) [32,43]. The XPS spectra of N1s for Fe@N₂-BC_{500–900} all exhibited three markedly fitted peaks at 398.5 eV , 400.0 eV and 401.2 eV (Fig. 4c–d), which can be assigned to pyridinic-N, pyrrolic-N and graphitic-N functional groups, respectively [26,32]. However, only weak peaks were found in the N1s XPS spectrum of Fe@N₀-BC_{500–900}. Usually, N atoms in biochar were lost due to decomposition with increasing pyrolysis temperature [37], and this was confirmed in this study. Furthermore, approximately 44–47% pyrrolic-N was converted into pyridinic-N and graphitic-N with increasing pyrolysis temperature, which would provide more defective N edges or sites in the biochar composite for nZVI loading [31,32].

The XPS spectra for Fe2p are shown in Fig. 4e–f, which exhibits two contributions (Fe2p_{3/2} and Fe2p_{1/2}) and four fitted peaks (711.0 , 712.9 , 724.6 and 726.5 eV , assigned to Fe(II)2p_{3/2}, Fe(III)2p_{3/2}, Fe(II)2p_{1/2} and Fe(III)2p_{1/2}, respectively) [44]. Moreover, the signals of Fe⁰ at 707.5 eV were also observed in all tested catalysts (Fig. 4e–f). These

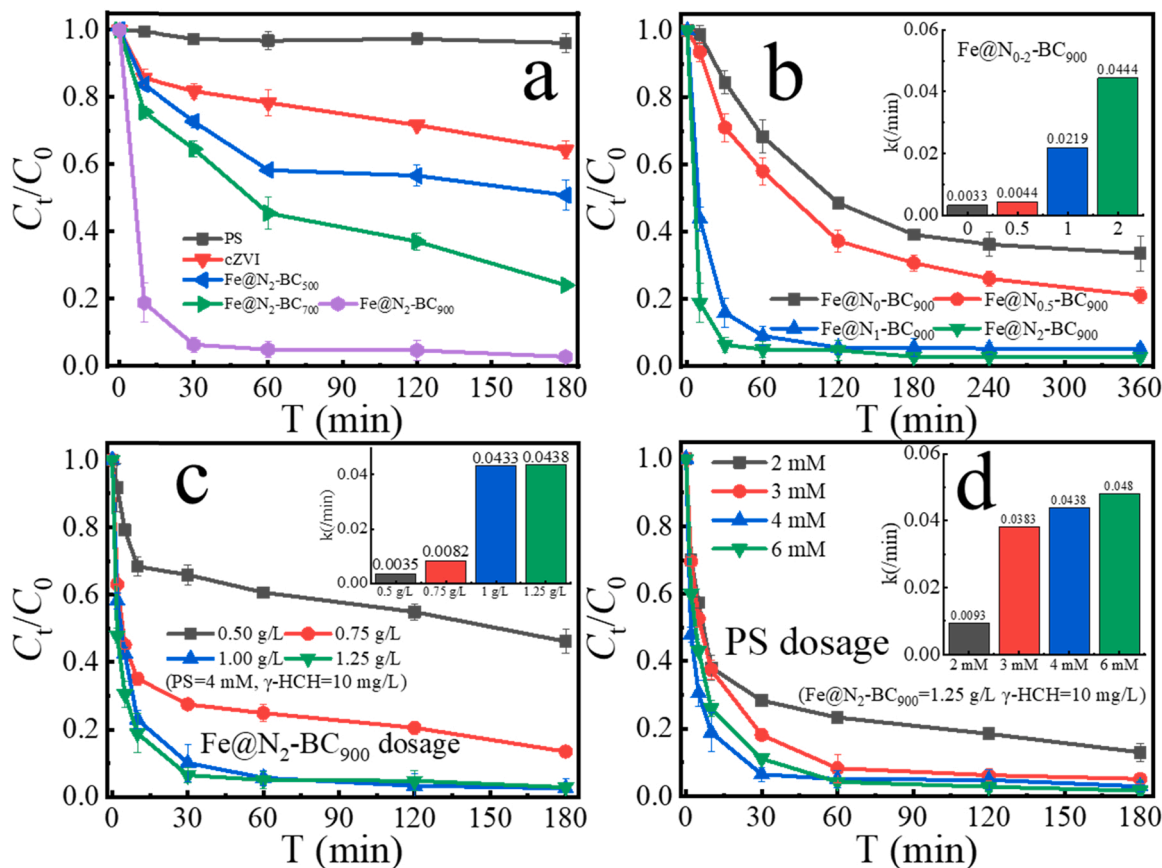


Fig. 5. Degradation kinetics of γ -HCH by different catalytic systems of Fe@N-BC/PS. Influences of catalyst type (a); N content (mass ratio of urea and pulp) (b); Fe@N₂-BC₉₀₀ dosage (c); PS dosage (d). (Reaction conditions: catalyst = 1.25 g/L, γ -HCH = 10 mg/L, PS = 4 mM, no adjustment of pH).

findings indicate that all composites contained Fe⁰ species, as the main component for these composites, however, Fe(II) and Fe(III) could also be observed due to the oxidation of nZVI by oxygen on the composite surface [10]. Notably, the relative content of Fe atoms on the Fe@N₂-BC₅₀₀₋₉₀₀ surface decreased from 8.48% to 5.16% with increasing pyrolysis temperature, which was opposite to the observed trend of the Fe@N₀-BC₅₀₀₋₉₀₀ composite that demonstrated an increase trend from 8.82% to 12.9%. In view of the similar bulk Fe content in these composites (42.6–50.8%; Table 1), this difference between the surface and bulk Fe contents might be caused by the greater number of carbon layers and pore channels of the biochar pyrolyzed at 900 °C, improving the formation and growth of nZVI at interior C layers and pores.

To further explain the effect of N-doping on the formation and growth of nZVI on biochar composite, the bulk and surface atomic ratios of Fe and C were calculated based on the bulk elemental analysis and XPS results (Tables 1 and S2). The surface Fe/C atomic ratios of the prepared composites with or without N-doping were all significantly less than their bulk Fe/C atomic ratios (Tables 1 and S2; $p < 0.01$). This suggests again that some nZVI was retained in the interior carbon layer and pore channel of the biochar, and their distribution on the composite surface declined, which is consistent with the decrease of specific surface area and porosity of Fe@N-BC after N-doping (Fig. S3 and Table S2). More importantly, the atomic ratio of Fe/C for Fe@N₂-BC₅₀₀₋₉₀₀ decreased significantly from 0.15 to 0.07 with increasing pyrolysis temperature, indicating that more nZVI tended to anchor in the carbon layer and pore structure instead of accumulating on the surface after N-doping. The opposite result from Fe@N₀-BC₅₀₀₋₉₀₀ further confirmed that N-doping promoted the growth and anchoring of nZVI in the pore structures of biochars. Additionally, the largest relative content of pyridinic-N (44.3%) and graphitic-N (36.2%) and the smallest surface

Fe/C value (0.07) of Fe@N₂-BC₉₀₀ further indicate the significance of N defect sites for the growth and anchoring of nZVI on/in the N-doped biochar.

3.3. Enhanced PS activation by Fe@N-BC composites for γ -HCH degradation

The degradation kinetics of γ -HCH by different catalytic systems in aqueous solution are shown in Figs. 5a and S1. The removal rates of γ -HCH within 180 min were only 4.7%, 7.5% and 19.9% by single PS, N₀-BC₉₀₀ and N₂-BC₉₀₀, respectively, suggesting that single PS or biochars with or without N-doping could hardly remove γ -HCH from the aqueous solution (Fig. S1). When Fe@N₂-BC₅₀₀₋₉₀₀ were applied together with PS as an activator, rapid degradation of γ -HCH was achieved with degradation rates of 41.6% by Fe@N₂-BC₅₀₀, 54.4% by Fe@N₂-BC₇₀₀ and 95.9% by Fe@N₂-BC₉₀₀ within 60 min (Fig. 5a). This confirms that these Fe@N-BCs could effectively activate PS and had greater γ -HCH degradation performance than cZVI (36.6%). It should be noted that 67.8% and 23.3% of γ -HCH were removed by the Fe@N₂-BC₉₀₀ and cZVI without PS within 180 min, respectively (Fig. S1). This indicates that Fe@N₂-BC₉₀₀ and cZVI can reduce γ -HCH, however, the degradation via reduction was not as efficient as the catalytic oxidation by PS. These findings further suggest that N-doped Fe@N₂-BC₉₀₀ could more effectively activate PS and then rapidly remove γ -HCH from the aqueous solution.

To clarify the effect of N-doping in Fe@N-BC on γ -HCH catalytic degradation, degradation experiments were conducted using Fe@N₀₋₂-BC₅₀₀₋₉₀₀. As shown in Figs. 5b and S6, with increasing mass ratios of N-dopant (urea), the degradation rates of γ -HCH by Fe@N₀₋₂-BC₅₀₀₋₉₀₀/PS oxidation increased. The degradation kinetics of γ -HCH were fitted by pseudo-first-order kinetics ($r^2 > 0.933$), and the k_{obs} values were

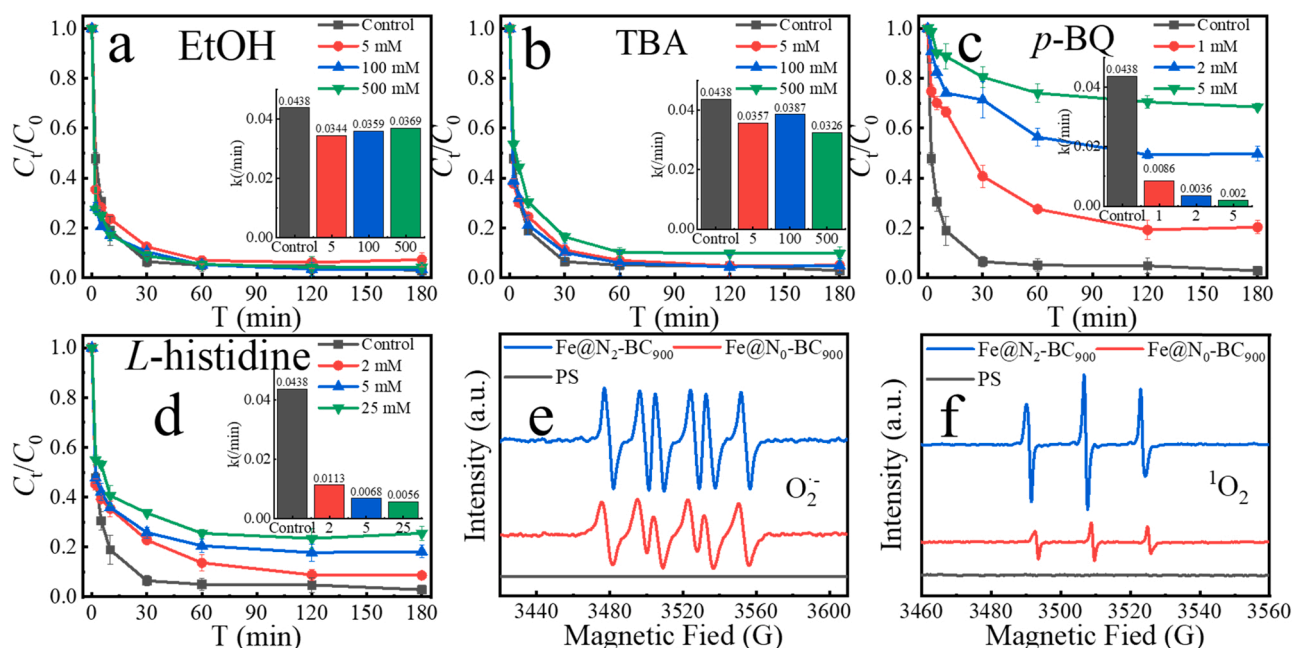


Fig. 6. Degradation kinetics of γ -HCH by Fe@N₂-BC₉₀₀/PS with different scavengers EtOH (a), TBA (b), *p*-BQ (c) and *L*-histidine (d). EPR spectra signals of $O_2^{\cdot -}$ (e) and 1O_2 (f) in Fe@N_{0.2}-BC₉₀₀/PS (reaction conditions: PS = 4 mM, Fe@N₂-BC₉₀₀ = 1.25 g/L, γ -HCH = 10 mg/L).

obtained (Figs. 5b and S6). The k_{obs} value of γ -HCH by Fe@N₂-BC₉₀₀/PS oxidation was 0.0444 min⁻¹, which was 13.5-fold, 10.1-fold and 2.0-fold that by Fe@N₀-BC₉₀₀/PS, Fe@N_{0.5}-BC₉₀₀/PS and Fe@N₁-BC₉₀₀/PS, respectively. This trend was also observed in Fe@N_{0.2}-BC_{500,700}/PS oxidation (Fig. S6). This is consistent with the results of bisphenol A degradation by Fe/N-codoped biochar-activated peroxymonosulfate oxidation reported by Xu et al. [36]. Furthermore, the k_{obs} values of γ -HCH by Fe@N_{0.2}-BC₅₀₀₋₉₀₀/PS oxidation also showed that better γ -HCH degradation performance was exhibited in the catalyst with greater graphitic-N and pyridine-N content. In summary, the increasing mass ratios of N-dopant in the precursor materials could significantly increase the graphitic-N and pyridine-N content in biochar, and then improve the catalytic performance of Fe@N-BCs for PS activation and significantly improve γ -HCH degradation. However, further increasing the percentage of N-dopant is not recommended since the enhancement of γ -HCH degradation became very small at high N-dopant dosage (Fig. 5b).

To optimize Fe@N₂-BC₉₀₀/PS oxidation of γ -HCH, γ -HCH degradation kinetics was evaluated using different Fe@N₂-BC₉₀₀ and PS dosages (Fig. 5c-d). As the Fe@N₂-BC₉₀₀ dosage increased from 0.5 g/L to 1.0 g/L, the degradation rates of γ -HCH within 60 min increased from 39.3% to 95.0%. The corresponding k_{obs} values increased from 0.0035 min⁻¹ to 0.0433 min⁻¹. However, further increasing of Fe@N₂-BC₉₀₀ dosage over 1.0 g/L only slightly enhanced k_{obs} values (0.0438 min⁻¹). The degradation of γ -HCH by Fe@N₂-BC₉₀₀/PS also increased with increasing PS dosage (2–6 mM) but the enhancement was rather limited (Fig. 5d). With the PS dosage increasing from 3 to 6 mM, the k_{obs} values of γ -HCH degradation only increased from 0.0383 min⁻¹ to 0.0480 min⁻¹. Previous literature has shown that in certain catalyst/PS systems with sufficient catalyst, a higher PS dosage usually means that a greater amount of PS is activated and more free radicals (e.g., $\bullet OH$, $SO_4^{\cdot -}$) are generated for pollutant degradation [3,32]. These above results suggest that an increase in Fe@N₂-BC₉₀₀ or PS dosage within a certain range was beneficial for γ -HCH degradation. In summary, an optimized system with 1.0 g/L catalyst and 4 mM oxidant (PS) for removing 10 mg/L HCH in aqueous solution was recommended.

Moreover, the optimized pH of γ -HCH degradation by Fe@N₂-BC₉₀₀/PS was 9.0, where γ -HCH degradation rate (97.2%) was greater than one at neutral pH (75.8%). The catalytic system had good tolerance in

water matrices with NO_3^- , Cl^- and HCO_3^- , while the catalytic performance was significantly inhibited by high concentrations of HA and $H_2PO_4^-$ (Fig. S7, Text S5). These show the promising application potentials of Fe@N₂-BC₉₀₀/PS for degradation of γ -HCH in actual contaminated water.

3.4. Mechanistic insights into γ -HCH degradation by Fe@N₂-BC₉₀₀/PS

3.4.1. The contribution of ROSs

To clarify the contributions of free radicals (e.g., $\bullet OH$, $SO_4^{\cdot -}$, $O_2^{\cdot -}$) and non-free radicals (1O_2) to γ -HCH degradation by Fe@N₂-BC₉₀₀/PS, quenching reactions with different scavengers (EtOH, TBA, *p*-BQ and *L*-histidine) were conducted. As shown in Fig. 6a–b, negligible effects for γ -HCH degradation were observed with the addition of EtOH and TBA in the reaction system, and the corresponding k_{obs} values declined by 15.7–21.5% and 11.6–25.6% with the addition of different concentrations of EtOH and TBA, respectively. This suggests that limited quantities $SO_4^{\cdot -}$ and $\bullet OH$ were generated in Fe@N₂-BC₉₀₀/PS and were not the dominant ROSs in γ -HCH degradation. Oppositely, strong inhibiting effects on γ -HCH degradation were observed with the addition of *p*-BQ and *L*-histidine, and such effects increased with increasing concentrations of the quenching reagents (Fig. 6c–d). This observation indicates that $O_2^{\cdot -}$ and 1O_2 both play important roles in γ -HCH degradation catalyzed by Fe@N₂-BC₉₀₀/PS. Furthermore, $O_2^{\cdot -}$ contributed more than 1O_2 to γ -HCH catalytic degradation as evidenced by the greater quenching effect of *p*-BQ and was considered to be a key factor in the ROS or non-free radical processes in PS-based AOPs [45]. Similar results were also reported in the literature by other researchers [26,32]. Opposite results for the quenching effects of *p*-BQ and *L*-histidine were obtained in Fe@N₀-BC₉₀₀/PS without N-doping (Fig. S8). This further suggests that N-doping can change the electron transfer mode of nZVI and biochar and lead to a different pathway for PS activation to produce $O_2^{\cdot -}$ and 1O_2 . The good dispersion and small particle size of the nZVI and N defects in the N-doped biochar can promote electron transfer from nZVI and N defects to PS molecules and break of O–O bonds in PS to produce $O_2^{\cdot -}$ [3,46]. Furthermore, $O_2^{\cdot -}$ can be transformed into 1O_2 in Fe@N₂-BC₉₀₀/PS by the N-doped sites in biochar, while *L*-histidine can capture 1O_2 to inhibit $O_2^{\cdot -}$ from attacking the γ -HCH molecule [26,32]. Thus, $O_2^{\cdot -}$ and 1O_2 were

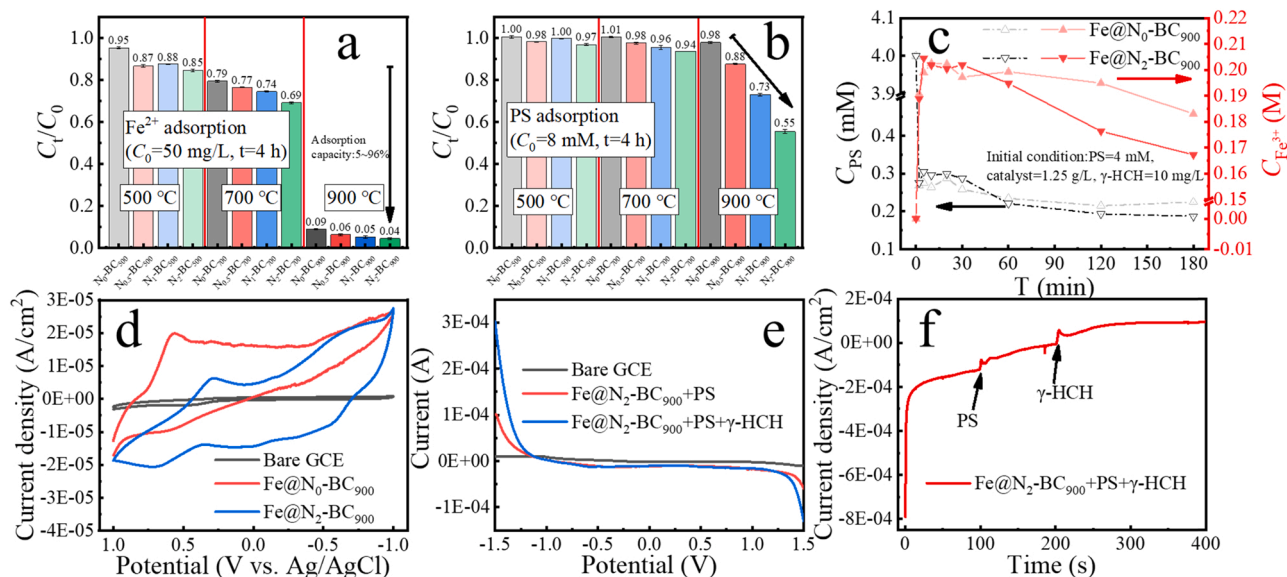
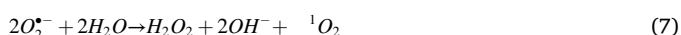


Fig. 7. The adsorption capacity of Fe@N-BC to Fe²⁺ (a) and PS (b); PS consumption and Fe³⁺ leaching (c); electrochemical evidence of CV (d), LSV curves (e) and I-t curves (obtained at 0.0 V vs. Ag/AgCl (50 mM Na₂SO₄)) (f) under different conditions.

mainly generated by the N-doped sites and nZVI and were the critical ROSs for the rapid γ-HCH catalytic degradation in Fe@N₂-BC₉₀₀/PS.

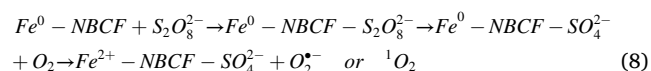
To further demonstrate the presence of free radical species or ¹O₂ in the γ-HCH catalytic degradation, EPR analysis was conducted for single PS and Fe@N_{0,2}-BC₉₀₀/PS with DMPO and TEMP for the capture of ROSs (SO₄^{•−}, •OH and O₂^{•−} and ¹O₂). No signals of SO₄^{•−} and •OH were observed in Fe@N_{0,2}-BC₉₀₀/PS (Fig. S9a), which was consistent with the free radical quenching results (Fig. 6). Whereas, typical signals of O₂^{•−} with a narrow six-line spectrum and ¹O₂ with a triplet peak in the EPR spectrum (1:1:1) were detected in both Fe@N₀-BC₉₀₀/PS and Fe@N₂-BC₉₀₀/PS (Fig. 6e–f). This evidence suggests again that the γ-HCH degradation was mainly resulted from the production of O₂^{•−} and ¹O₂ in Fe@N₂-BC₉₀₀/PS. Previous literature has reported that ¹O₂ is an important ROS and can be converted from O₂^{•−} in PS-based AOPs [47]; and these species both play vital roles in the free radical and non-free radical pathways of AOPs for pollutant degradation [3,37,45]. However, weak signals of SO₄^{•−} and •OH and no signals of O₂^{•−} and ¹O₂ were observed in N₀-BC₉₀₀/PS and N₂-BC₉₀₀/PS without nZVI (Fig. S9a–b), which were different from the results of Fe@N_{0,2}-BC₉₀₀/PS. This difference may be due to that the persistent free radicals in biochar (N_{0,2}-BC₉₀₀) could activate PS to generate SO₄^{•−} and •OH, however, the excess transition metal ion in Fe@N_{0,2}-BC₉₀₀/PS would consume the persistent free radicals [7,48]. Thus, we can conclude that the production of O₂^{•−} and ¹O₂ were the main ROSs governing the γ-HCH catalytic degradation in Fe@N₂-BC₉₀₀/PS, and the generation of O₂^{•−} and ¹O₂ can be summarized by the following proposed redox reactions (Eqs. (2–7)).



3.4.2. Nonradical pathway depending on electronic transfer

Prior to electrochemical experiments, the adsorption of Fe²⁺

(0.89 mM) and PS (8 mM) on different biochars with or without N-doping was evaluated (Fig. 7a–b). The results showed that the amount of adsorbed Fe²⁺ and PS on N-doped biochars significantly increased with increasing N content in the N-doped biochars. This evidences that the N-doped active sites on biochar could enhance the adsorption capacity for Fe²⁺ and PS and further improve the distribution of Fe²⁺ and PS in the solid-liquid reaction system, especially for N₂-BC₉₀₀. Fe³⁺ leaching and PS consumption experimental results showed that Fe@N₂-BC₉₀₀ could significantly suppress Fe³⁺ leaching and accelerate the consumption of PS (Fig. 7c), while such effects were not obtained in Fe@N₂-BC₇₀₀/PS (Fig. S10). Thus, nZVI and PS reacted closely and rapidly at the interface of N₂-BC₉₀₀ by N-doped sites and then strongly promoted electron transfer, which provided an additional nonradical pathway for γ-HCH degradation by Fe@N₂-BC₉₀₀/PS. Additionally, due to the presence of N defects (pyridinic-N and graphitic-N), direct electron transfer from the nZVI to the PS via of N-doped sites in biochar, may preferentially occur in Fe@N₂-BC₉₀₀/PS, where nZVI acts as an electron donor group, and the N-doped biochar framework (NBCF) serves as electron transfer channels for activating PS to produce extra ROSs (Eq. (8)).



To further verify the electron transfer process in Fe@N₂-BC₉₀₀/PS, its electrochemical performance was observed in a three-electrode configuration. The cyclic voltammetry curves of Fe@N_{0,2}-BC₉₀₀ are depicted in Fig. 7d. Compared with the control group (a bare glassy carbon electrode (GCE)), significantly increased current densities and redox peaks were both observed in Fe@N₀-BC₉₀₀/PS and Fe@N₂-BC₉₀₀/PS, confirming the presence of N-doped biochar as a beneficial carrier for electron transfer and redox reactions. Notably, compared to Fe@N₀-BC₉₀₀, Fe@N₂-BC₉₀₀ had a greater difference in charge potential and better cycle reversibility. This difference may have been caused by the small, well-distributed nZVI particles on the surface or nZVI in the carbon layer and pore channel of Fe@N₂-BC₉₀₀, which improves the electron transfer and reaction activity. In contrast, without N-doping, a large amount of nZVI agglomerated on the biochar surface, limiting electron transfer and leading to a lower reaction activity [49]. Moreover, linear sweep voltammetry was further examined and is presented in Fig. 7e. The electric current significantly increased with the addition of PS, suggesting that more electron transfer reactions occurred in the activation process of PS. Previous literature ascribed this phenomenon

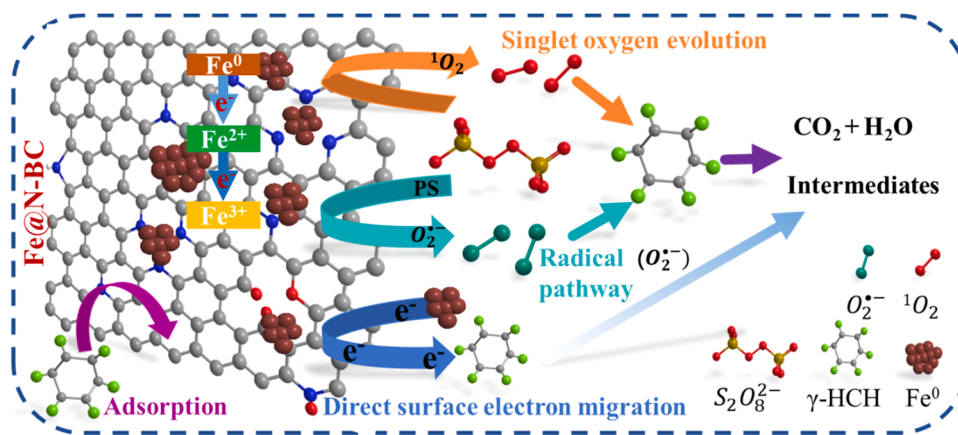


Fig. 8. Mechanism scheme of γ -HCH removal in Fe@N₂-BC₉₀₀/PS.

to the formation of metastable reactive complexes between the active sites on activators and PS molecules [32,46]. In addition, chronoamperometry (I-t curve) was used to test the current output of electron transfer in Fe@N₂-BC₉₀₀/PS. As shown in Fig. 7f, significant current peaks were observed when 4 mM PS was added at 100 s and γ -HCH was injected at 200 s. This suggests that the electron transfer process was caused by the interaction between PS and Fe@N₂-BC₉₀₀ in the catalytic system, and γ -HCH molecules were attacked by the produced ROSs and electrons. Thus, electron transfer occurred in Fe@N₂-BC₉₀₀/PS, and this capacity for biochar was enhanced by N-doping.

3.4.3. Reaction mechanism

Based on the comprehensive results of catalyst performance, quenching and electrochemical tests, the possible mechanism for γ -HCH degradation in Fe@N₂-BC₉₀₀/PS was proposed (Fig. 8). It can be concluded that the ROS reaction and electron transfer process were both the primary mechanisms for γ -HCH degradation by Fe@N₂-BC₉₀₀/PS. ROSs, mainly O₂^{•-} and ¹O₂, were produced by the redox reaction between PS and the catalyst, which attacked γ -HCH molecules and led to the radical/nonradical pathways for its degradation. However, direct surface electron transfer to the γ -HCH and PS molecules also occurred on the catalyst surface by using biochar as an electronic channel; this process was enhanced by the N-doping modification. The ROS reaction and electron transfer pathway work together, resulting in effective γ -HCH degradation in Fe@N₂-BC₉₀₀/PS.

4. Conclusions

In this study, novel Fe@N-BCs were successfully synthesized and applied as PS activators for γ -HCH degradation in aqueous solution. The N-doped defects in biochar could improve the anchor, dispersion and loading of nZVI and greatly enhance the PS activation and γ -HCH degradation, which can be summarized as follows: (i) N-doped biochar served as a better carrier, restrained the agglomeration and oxidation of nZVI, promoted the growth, anchor and dispersion of nZVI, and induced the formation of uniform and amorphous nZVI with a particle size of <100 nm (diameter); (ii) more N-doped defects (e.g., graphitic-N and pyridine-N) were present in biochar after N-doping, which could activate PS to produce more ROSs (O₂^{•-} and ¹O₂) and improve the catalytic performance; and (iii) N-doped biochar mediated the electron transfer and accelerated the transfer of electrons from nZVI to PS, which improved the PS activation of Fe@N-BCs by nonradical pathways. Benefiting from these above synergistic effects between N-doped biochar and nZVI, the resulting Fe@N₂-BC₉₀₀ presented excellent catalytic activity for PS activation, with a k_{obs} value for γ -HCH degradation of 0.0444 min⁻¹, which was 13.5-fold that of Fe@N₀-BC₉₀₀/PS without N-doping, respectively. Furthermore, the Fe@N-BC catalysts showed effectiveness

over a wide pH range and had good tolerance in water matrices with NO₃⁻, Cl⁻ and HCO₃⁻, while the catalytic performance was significantly inhibited by high concentrations of HA and H₂PO₄⁻. This work provides a new approach by using low mass of N-dopants during biochar pyrolysis to generate nZVI/N-BCs for PS activation in pollution control, and also tested and verified the synergistic effects of Fe and N elements in the PS-based AOPs. The degradation mechanisms of γ -HCH were systematically explored and a new mechanism of electron transfer was proposed.

CRedit authorship contribution statement

Peng Huang: Methodology, Investigation, Writing – original draft. **Peng Zhang:** Methodology, Investigation, Writing – review & editing and Funding acquisition. **Cuiping Wang and Jingchun Tang:** Methodology, Writing – review & editing. **Hongwen Sun:** Writing – review & editing, Funding acquisition.

Declaration of Competing Interest

The authors declare no competing financial interest.

Acknowledgements

This work was supported by the National Key R&D Program of China (2018YFC1802001), Science and Technology Major Project of Tianjin (18ZXSZSF00110), Key R&D Program from Science and Technology Department of Ningxia (2019BFG02020), Key R&D Program of Shandong Province (2021CXGC011206), Ministry of Education of China (T2017002) and Postgraduate Research Innovation Project of Tianjin (2020YJSB059).

Appendix A. Supporting information

Supplementary data associated with this article can be found in the online version at doi:10.1016/j.apcatb.2021.120926.

References

- [1] X. Duan, H. Sun, Z. Shao, S. Wang, Nonradical reactions in environmental remediation processes: Uncertainty and challenges, Appl. Catal. B 224 (2018) 973–982, <https://doi.org/10.1016/j.apcatb.2017.11.051>.
- [2] B.C. Hodges, E.L. Cates, J.H. Kim, Challenges and prospects of advanced oxidation water treatment processes using catalytic nanomaterials, Nat. Nanotechnol. 13 (2018) 642–650, <https://doi.org/10.1038/s41565-018-0216-x>.
- [3] J. Lee, U. von Gunten, J.H. Kim, Persulfate-based advanced oxidation: critical assessment of opportunities and roadblocks, Environ. Sci. Technol. 54 (2020) 3064–3081, <https://doi.org/10.1021/acs.est.9b07082>.
- [4] I.A. Ike, K.G. Linden, J.D. Orbell, M. Duke, Critical review of the science and sustainability of persulfate advanced oxidation processes, Chem. Eng. J. 338 (2018) 651–669, <https://doi.org/10.1016/j.cej.2018.01.034>.

- [5] J.L. Wang, S.Z. Wang, Activation of persulfate (PS) and peroxymonosulfate (PMS) and application for the degradation of emerging contaminants, *Chem. Eng. J.* 334 (2018) 1502–1517, <https://doi.org/10.1016/j.cej.2017.11.059>.
- [6] W.D. Oh, Z.L. Dong, T.T. Lim, Generation of sulfate radical through heterogeneous catalysis for organic contaminants removal: current development, challenges and prospects, *Appl. Catal. B* 194 (2016) 169–201, <https://doi.org/10.1016/j.apcatb.2016.04.003>.
- [7] G. Zhao, J. Zou, X. Chen, L. Liu, Y. Wang, S. Zhou, X. Long, J. Yu, F. Jiao, Iron-based catalysts for persulfate-based advanced oxidation process: microstructure, property and tailoring, *Chem. Eng. J.* (2020), 127845, <https://doi.org/10.1016/j.cej.2020.127845>.
- [8] X. Yi, H. Ji, C. Wang, Y. Li, Y. Li, C. Zhao, A. Wang, H. Fu, P. Wang, X. Zhao, W. Liu, Photocatalysis-activated SR-AOP over PDINH/MIL-88A(Fe) composites for boosted chloroquine phosphate degradation: Performance, mechanism, pathway and DFT calculations, *Appl. Catal. B* 293 (2021), 120229, <https://doi.org/10.1016/j.apcatb.2021.120229>.
- [9] Y. Sun, J. Li, T. Huang, X. Guan, The influences of iron characteristics, operating conditions and solution chemistry on contaminants removal by zero-valent iron: a review, *Water Res.* 100 (2016) 277–295, <https://doi.org/10.1016/j.watres.2016.05.031>.
- [10] M. Stefaniuk, P. Oleszczuk, Y.S. Ok, Review on nano zerovalent iron (nZVI): from synthesis to environmental applications, *Chem. Eng. J.* 287 (2016) 618–632, <https://doi.org/10.1016/j.cej.2015.11.046>.
- [11] W. Wang, H. Wang, G. Li, T. An, H. Zhao, P.K. Wong, Catalyst-free activation of persulfate by visible light for water disinfection: efficiency and mechanisms, *Water Res.* 157 (2019) 106–118, <https://doi.org/10.1016/j.watres.2019.03.071>.
- [12] W. Wang, H. Wang, G. Li, P.K. Wong, T. An, Visible light activation of persulfate by magnetic hydrochar for bacterial inactivation: efficiency, recyclability and mechanisms, *Water Res.* 176 (2020), 115746, <https://doi.org/10.1016/j.watres.2020.115746>.
- [13] C. Kim, J.Y. Ahn, T.Y. Kim, W.S. Shin, I. Hwang, Activation of persulfate by nanosized zero-valent iron (nZVI): Mechanisms and transformation products of nZVI, *Environ. Sci. Technol.* 52 (2018) 3625–3633, <https://doi.org/10.1021/acs.est.7b05847>.
- [14] S. Xiao, M. Cheng, H. Zhong, Z.F. Liu, Y. Liu, X. Yang, Q.H. Liang, Iron-mediated activation of persulfate and peroxymonosulfate in both homogeneous and heterogeneous ways: a review, *Chem. Eng. J.* 384 (2020), 123265, <https://doi.org/10.1016/j.cej.2019.123265>.
- [15] S. Rodriguez, A. Santos, A. Romero, Oxidation of priority and emerging pollutants with persulfate activated by iron: effect of iron valence and particle size, *Chem. Eng. J.* 318 (2017) 197–205, <https://doi.org/10.1016/j.cej.2016.06.057>.
- [16] S.H. Wu, H.J. He, X. Li, C.P. Yang, G.M. Zeng, B. Wu, S.Y. He, L. Lu, Insights into atrazine degradation by persulfate activation using composite of nanoscale zero-valent iron and graphene: performances and mechanisms, *Chem. Eng. J.* 341 (2018) 126–136, <https://doi.org/10.1016/j.cej.2018.01.136>.
- [17] B.W. Zhang, Y. Guo, J.Y. Huo, H.J. Xie, C.H. Xu, S. Liang, Combining chemical oxidation and bioremediation for petroleum polluted soil remediation by BC-nZVI activated persulfate, *Chem. Eng. J.* 382 (2020), 123055, <https://doi.org/10.1016/j.cej.2019.123055>.
- [18] X. Jiang, Y. Guo, L. Zhang, W. Jiang, R. Xie, Catalytic degradation of tetracycline hydrochloride by persulfate activated with nano Fe⁰ immobilized mesoporous carbon, *Chem. Eng. J.* 341 (2018) 392–401, <https://doi.org/10.1016/j.cej.2018.02.034>.
- [19] J. Yu, X. Hou, X. Hu, H. Yuan, J. Wang, C. Chen, Efficient degradation of chloramphenicol by zero-valent iron microspheres and new insights in mechanisms, *Appl. Catal., B* 256 (2019), 117876, <https://doi.org/10.1016/j.apcatb.2019.117876>.
- [20] K.V.K. Ansaf, S. Ambika, I.M. Nambi, Performance enhancement of zero valent iron based systems using depassivators: optimization and kinetic mechanisms, *Water Res.* 102 (2016) 436–444, <https://doi.org/10.1016/j.watres.2016.06.064>.
- [21] R. Pereira Lopes, D. Astruc, Biochar as a support for nanocatalysts and other reagents: recent advances and applications, *Coord. Chem. Rev.* 426 (2021), 213585, <https://doi.org/10.1016/j.ccr.2020.213585>.
- [22] W. Chen, J. Meng, X. Han, Y. Lan, W. Zhang, Past, present, and future of biochar, *Biochar 1* (2019) 75–87, <https://doi.org/10.1007/s42773-019-00008-3>.
- [23] P. Wu, S.T. Ata-Ul-Karim, B.P. Singh, H. Wang, T. Wu, C. Liu, G. Fang, D. Zhou, Y. Wang, W. Chen, A scientometric review of biochar research in the past 20 years (1998–2018), *Biochar 1* (2019) 23–43, <https://doi.org/10.1007/s42773-019-00002-9>.
- [24] R.Z. Wang, D.L. Huang, Y.G. Liu, C. Zhang, C. Lai, X. Wang, G.M. Zeng, X.M. Gong, A. Duan, Q. Zhang, P. Xu, Recent advances in biochar-based catalysts: properties, applications and mechanisms for pollution remediation, *Chem. Eng. J.* 371 (2019) 380–403, <https://doi.org/10.1016/j.cej.2019.04.071>.
- [25] J. Yan, L. Han, W. Gao, S. Xue, M. Chen, Biochar supported nanoscale zerovalent iron composite used as persulfate activator for removing trichloroethylene, *Bioresour. Technol.* 175 (2015) 269–274, <https://doi.org/10.1016/j.biortech.2014.10.103>.
- [26] X. Li, Y. Jia, M. Zhou, X. Su, J. Sun, High-efficiency degradation of organic pollutants with Fe, N co-doped biochar catalysts via persulfate activation, *J. Hazard. Mater.* 397 (2020), 122764, <https://doi.org/10.1016/j.jhazmat.2020.122764>.
- [27] L. Yang, Y. Chen, D. Ouyang, J.C. Yan, L.B. Qian, L. Han, M.F. Chen, J. Li, M.Y. Gu, Mechanistic insights into adsorptive and oxidative removal of monochlorobenzene in biochar-supported nanoscale zero-valent iron/persulfate system, *Chem. Eng. J.* 400 (2020), 125811, <https://doi.org/10.1016/j.cej.2020.125811>.
- [28] L. Tang, Y. Liu, J. Wang, G. Zeng, Y. Deng, H. Dong, H. Feng, J. Wang, B. Peng, Enhanced activation process of persulfate by mesoporous carbon for degradation of aqueous organic pollutants: electron transfer mechanism, *Appl. Catal. B* 231 (2018) 1–10, <https://doi.org/10.1016/j.apcatb.2018.02.059>.
- [29] M. Zhang, L. Shu, X. Shen, X. Guo, S. Tao, B. Xing, X. Wang, Characterization of nitrogen-rich biomaterial-derived biochars and their sorption for aromatic compounds, *Environ. Pollut.* 195 (2014) 84–90, <https://doi.org/10.1016/j.envpol.2014.08.018>.
- [30] L. Leng, L. Yang, S. Leng, W. Zhang, Y. Zhou, H. Peng, H. Li, Y. Hu, S. Jiang, H. Li, A review on nitrogen transformation in hydrochar during hydrothermal carbonization of biomass containing nitrogen, *Sci. Total Environ.* 756 (2021), 143679, <https://doi.org/10.1016/j.scitotenv.2020.143679>.
- [31] W. Ren, G. Nie, P. Zhou, H. Zhang, X. Duan, S. Wang, The intrinsic nature of persulfate activation and N-doping in carbocatalysis, *Environ. Sci. Technol.* 54 (2020) 6438–6447, <https://doi.org/10.1021/acs.est.0c01161>.
- [32] C. Chen, T.F. Ma, Y.N. Shang, B.Y. Gao, B. Jin, H.B. Dan, Q. Li, Q.Y. Yue, Y.W. Li, Y. Wang, X. Xu, In-situ pyrolysis of Enteromorpha as carbocatalyst for catalytic removal of organic contaminants: Considering the intrinsic N/Fe in Enteromorpha and non-radical reaction, *Appl. Catal. B* 250 (2019) 382–395, <https://doi.org/10.1016/j.apcatb.2019.03.048>.
- [33] X. Li, X. Huang, S. Xi, S. Miao, J. Ding, W. Cai, S. Liu, X. Yang, H. Yang, J. Gao, J. Wang, Y. Huang, T. Zhang, B. Liu, Single cobalt atoms anchored on porous N-doped graphene with dual reaction sites for efficient Fenton-like catalysis, *J. Am. Chem. Soc.* 140 (2018) 12469–12475, <https://doi.org/10.1021/jacs.8b05992>.
- [34] S. Zhu, X. Huang, F. Ma, L. Wang, X. Duan, S. Wang, Catalytic removal of aqueous contaminants on N-doped graphitic biochars: Inherent roles of adsorption and nonradical mechanisms, *Environ. Sci. Technol.* 52 (2018) 8649–8658, <https://doi.org/10.1021/acs.est.8b01817>.
- [35] S. Cai, Q. Zhang, Z. Wang, S. Hua, D. Ding, T. Cai, R. Zhang, Pyrrolic N-rich biochar without exogenous nitrogen doping as a functional material for bisphenol A removal: performance and mechanism, *Appl. Catal. B* 291 (2021), 120093, <https://doi.org/10.1016/j.apcatb.2021.120093>.
- [36] L. Xu, B.R. Fu, Y. Sun, P.K. Jin, X. Bai, X. Jin, X. Shi, Y. Wang, S.T. Nie, Degradation of organic pollutants by Fe/N co-doped biochar via peroxymonosulfate activation: Synthesis, performance, mechanism and its potential for practical application, *Chem. Eng. J.* 400 (2020), 125870, <https://doi.org/10.1016/j.cej.2020.125870>.
- [37] Y.L. Cao, S.J. Mao, M.M. Li, Y.Q. Chen, Y. Wang, Metal/porous carbon composites for heterogeneous catalysis: Old catalysts with improved performance promoted by N-doping, *ACS Catal.* 7 (2017) 8090–8112, <https://doi.org/10.1021/acscatal.7b02335>.
- [38] P. Huang, P. Zhang, L. Min, J. Tang, H. Sun, Synthesis of cellulose carbon aerogel via combined technology of wet ball-milling and TEMPO-mediated oxidation and its supersorption performance to ionic dyes, *Bioresour. Technol.* 315 (2020), 123815, <https://doi.org/10.1016/j.biortech.2020.123815>.
- [39] S.C. Li, B.C. Hu, Y.W. Ding, H.W. Liang, C. Li, Z.Y. Yu, Z.Y. Wu, W.S. Chen, S.H. Yu, Wood-derived ultrathin carbon nanofiber aerogels, *Angew. Chem. Int. Ed. Engl.* 57 (2018) 7085–7090, <https://doi.org/10.1002/anie.201802753>.
- [40] H. Su, Z. Fang, P.E. Tsang, L. Zheng, W. Cheng, J. Fang, D. Zhao, Remediation of hexavalent chromium contaminated soil by biochar-supported zero-valent iron nanoparticles, *J. Hazard. Mater.* 318 (2016) 533–540, <https://doi.org/10.1016/j.jhazmat.2016.07.039>.
- [41] C. Liang, C.F. Huang, N. Mohanty, R.M. Kurakalva, A rapid spectrophotometric determination of persulfate anion in ISCO, *Chemosphere* 73 (2008) 1540–1543, <https://doi.org/10.1016/j.chemosphere.2008.08.043>.
- [42] W.J. Shen, X.M. Wang, F.L. Jia, Z. Tong, H.W. Sun, X.B. Wang, F.H. Song, Z.H. Ai, L.Z. Zhang, B. Chai, Amorphization enables highly efficient anaerobic thiophenol reduction by zero-valent iron, *Appl. Catal. B* 264 (2020), 118550, <https://doi.org/10.1016/j.apcatb.2019.118550>.
- [43] J. Kang, X.G. Duan, C. Wang, H.Q. Sun, X.Y. Tan, M.O. Tade, S.B. Wang, Nitrogen-doped bamboo-like carbon nanotubes with Ni encapsulation for persulfate activation to remove emerging contaminants with excellent catalytic stability, *Chem. Eng. J.* 332 (2018) 398–408, <https://doi.org/10.1016/j.cej.2017.09.102>.
- [44] Y. Sun, Z.X. Yang, P.F. Tian, Y.Y. Sheng, J. Xu, Y.F. Han, Oxidative degradation of nitrobenzene by a Fenton-like reaction with Fe-Cu bimetallic catalysts, *Appl. Catal. B* 244 (2019) 1–10, <https://doi.org/10.1016/j.apcatb.2018.11.009>.
- [45] L. Wang, X. Lan, W. Peng, Z. Wang, Uncertainty and misinterpretation over identification, quantification and transformation of reactive species generated in catalytic oxidation processes: a review, *J. Hazard. Mater.* 408 (2021), 124436, <https://doi.org/10.1016/j.jhazmat.2020.124436>.
- [46] P.J. Duan, Y.F. Qi, S.S. Feng, X.M. Peng, W. Wang, Y. Yue, Y. Shang, Y.W. Li, B. Y. Gao, X. Xu, Enhanced degradation of clothianidin in peroxymonosulfate/catalyst system via core-shell FeMn @ N-C and phosphate surrounding, *Appl. Catal. B* 267 (2020), 118717, <https://doi.org/10.1016/j.apcatb.2020.118717>.
- [47] X. Zhang, F. Wang, C. Wang, P. Wang, H. Fu, C. Zhao, Photocatalysis activation of peroxodisulfate over the supported Fe₃O₄ catalyst derived from MIL-88A(Fe) for efficient tetracycline hydrochloride degradation, *Chem. Eng. J.* 426 (2021), 131927, <https://doi.org/10.1016/j.cej.2021.131927>.
- [48] G. Fang, C. Liu, J. Gao, D.D. Dionysiou, D. Zhou, Manipulation of persistent free radicals in biochar to activate persulfate for contaminant degradation, *Environ. Sci. Technol.* 49 (2015) 5645–5653, <https://doi.org/10.1021/es5061512>.
- [49] Z.B. Liang, W. Xia, C. Qu, B. Qiu, H. Tabassum, S. Gao, R.Q. Zou, Edge-abundant porous Fe₃O₄ nanoparticles docking in nitrogen-rich graphene aerogel as efficient and durable electrocatalyst for oxygen reduction, *ChemElectroChem* 4 (2017) 2442–2447, <https://doi.org/10.1002/celec.201700627>.